

Self-supervised driven consistency training for annotation efficient histopathology image analysis

Chetan L. Srinidhi^{a,b,*}, Seung Wook Kim^c, Fu-Der Chen^d, Anne L. Martel^{a,b}

^aPhysical Sciences, Sunnybrook Research Institute, Toronto, Canada

^bDepartment of Medical Biophysics, University of Toronto, Canada

^cDepartment of Computer Science, University of Toronto, Canada

^dDepartment of Electrical & Computer Engineering, University of Toronto, Canada

Abstract

Training a neural network with a large labeled dataset is still a dominant paradigm in computational histopathology. However, obtaining such exhaustive manual annotations is often expensive, laborious, and prone to inter and intra-observer variability. While recent self-supervised and semi-supervised methods can alleviate this need by learning unsupervised feature representations, they still struggle to generalize well to downstream tasks when the number of labeled instances is small. In this work, we overcome this challenge by leveraging both *task-agnostic* and *task-specific* unlabeled data based on two novel strategies: i) a self-supervised pretext task that harnesses the underlying multi-resolution contextual cues in histology whole-slide images to learn a powerful supervisory signal for unsupervised representation learning; ii) a new *teacher-student* semi-supervised consistency paradigm that learns to effectively transfer the pretrained representations to downstream tasks based on prediction consistency with the task-specific unlabeled data.

We carry out extensive validation experiments on three histopathology benchmark datasets across two classification and one regression based tasks, *i.e.*, tumor metastasis detection, tissue type classification, and tumor cellularity quantification. Under limited-label data, the proposed method yields tangible improvements, which is close to or even outperforming other state-of-the-art self-supervised and supervised baselines. Furthermore, we empirically show that the idea of bootstrapping the self-supervised pretrained features is an effective way to improve the task-specific semi-supervised learning on standard benchmarks. Code and pretrained models are made available at: https://github.com/srinidhiPY/SSL_CR_Histo

Keywords: Self-supervised learning, Semi-supervised learning, Limited annotations, Histopathology image analysis, Digital pathology

1. Introduction

Deep neural network models have achieved tremendous success in obtaining state-of-the-art performance on various histology image analysis tasks ranging from disease grading, cancer classification to outcome pre-

diction (Srinidhi et al., 2021; Bera et al., 2019; Litjens et al., 2017). The main success of these methods is attributed to the availability of large-scale open datasets with clean manual annotations. However, collecting such a large corpus of labeled data is often expensive, laborious, and requires skillful domain expertise, notably in the histopathology domain (Madabhushi and Lee, 2016). Recently, self-supervised and semi-supervised approaches are becoming increasingly popular to alleviate the anno-

*Corresponding author:
E-mail address: chetan.srinidhi@utoronto.ca (Chetan L. Srinidhi)

tation burden by leveraging the readily available unlabeled data that can be trained with limited supervision. These methods have recently demonstrated promising results on various computer vision (Jing and Tian, 2020; Laine and Aila, 2016; Sohn et al., 2020) and medical image analysis tasks (Chen et al., 2019; Tellez et al., 2019b; Li et al., 2020c). In this paper, we focus on the self-supervised driven semi-supervised learning paradigm for histopathology image analysis by efficiently exploiting the underlying information present in unlabeled data, both in *task-agnostic* and *task-specific* ways.

The existing plethora of self-supervised learning (SSL) methods can be viewed as defining a surrogate task, i.e., a *pretext* task - which is formulated using only unlabeled examples and which requires a high-level semantic understanding of the image to solve the pretext tasks (Jing and Tian, 2020). The neural network model trained to solve this pretext task often learns useful visual representations that can be transferred to any *downstream* task to solve the task-specific problem. On the other hand, another important stream of work is based on semi-supervised learning (SmSL), which seeks to learn from both labeled and unlabeled examples with limited manual annotations (Chapelle et al., 2010). Among SmSL methods, the most recent and popular stream of approaches are based on *consistency* regularization (Laine and Aila, 2016; Sajjadi et al., 2016) and *pseudo labeling* (Lee, 2013; Sohn et al., 2020) techniques. The consistency based methods aim to constrain network predictions to be invariant to input or model weight perturbations, such as image augmentations (Xie et al., 2019), network dropout (Srivastava et al., 2014) and stochastic depth (Huang et al., 2016). The main idea is that the model should predict similar labels for both the input image and its perturbed (augmented) version of the same image. Alternatively, pseudo labeling based methods impute artificial (pseudo labels) for the unlabeled data obtained from the model class predictions, which is trained using labeled data alone (Sohn et al., 2020). The success of these SmSL approaches is attributed to the fact that these models implicitly learn to fit decision boundaries by grouping similar images to share similar labels, forming high-density clusters in the input feature space.

Despite significant advancements among SSL and SmSL approaches, they still suffer from some major limitations. Several SSL methods assume that optimizing

the pretext objective task will invariably yield suitable downstream representations for the target task. However, many recent studies (Zoph et al., 2020; Yan et al., 2020; Goyal et al., 2019) have shown that SSL methods overfit to the pretraining objective and may not generalize well to the downstream tasks. In contrast, methods based on SmSL approaches generally struggle to learn effectively when the number of labeled instances are scarce and also noisy (Rebuffi et al., 2020). This is a typical scenario in histopathology, where the number of manually labeled annotations is small and are often noisy (Shi et al., 2020). Besides, when the ratio of labeled and unlabeled samples is highly imbalanced, models trained solely based on consistency strategy have very low accuracy and higher entropy, which prevents them from achieving high-confidence scores (i.e., pseudo labels) on unlabeled data (Kim et al., 2020). To address these shortcomings, several recent studies (Zhai et al., 2019; Rebuffi et al., 2020) have explored the feasibility of integrating the merits of both SSL and SmSL approaches to further enhance the performance on downstream tasks by efficiently exploiting the limited labeled data together with abundant unlabeled data. These approaches first aim to initialize a good latent representation of the data using self-supervised pretraining, followed by reinitializing these features on downstream tasks in a task-specific semi-supervised manner. This idea of bootstrapping features trained via SSL algorithm has been shown to improve the SmSL approach by preventing overfitting on the target domain (Zhai et al., 2019).

In this paper, we take inspiration from the above observations and propose a novel self-supervised driven semi-supervised learning framework for histopathology image analysis, which leverages the unlabeled data both in a task-agnostic and task-specific manner. To this end, we first present a simple yet effective, self-supervised pretext task, namely, **Resolution Sequence Prediction (RSP)**, which leverages the multi-resolution contextual information present in the pyramidal nature of histology whole-slide images (WSI’s). Our design choice is inspired by the way a pathologist searches for cancerous regions in a WSI. Typically, a pathologist zooms in and out into each region, where the tissue is examined at high to low resolution to obtain the details of individual cells and their surroundings. In this work, we show that exploiting such meaningful multi-resolution contextual informa-

tion provides a powerful surrogate supervisory signal for unsupervised representation learning. Second, we further develop a ‘*teacher-student*’ semi-supervised consistency paradigm by efficiently transferring the self-supervised pretrained representations to downstream tasks. Our approach can be viewed as a knowledge distillation method (Hinton et al., 2015), where the self-supervised teacher model learns to generate pseudo labels for the task-specific unlabeled data, which forces the student model to make predictions consistent with the teacher model. We experimentally show that initializing the student model with the SSL pretrained teacher model achieves robustness against noisy input data (i.e., *noise* is injected through various kinds of domain-specific augmentations) and helps learn faster than the teacher in practice. Our whole framework is trained end-to-end to seamlessly integrate the information present in labeled and unlabeled data both in task-specific and task-agnostic ways.

The major contributions of this paper are:

- We propose a novel self-supervised pretext task for generating unsupervised visual representations via predicting the resolution sequence ordering in the pyramidal structure of histology WSI.
- We present a new ‘teacher-student’ semi-supervised consistency paradigm by efficiently transferring the self-supervised pretrained representations to downstream tasks based on prediction consistency with the task-specific unlabeled data.
- We extensively validate our method on three benchmark datasets across two classification and one regression based histopathology tasks, i.e., tumor metastasis detection, tissue type classification, and tumor cellularity quantification. The proposed self-supervised method, along with consistency training, is shown to improve the performance on all three datasets, especially in the less annotated data regime.

The paper is organized as follows: we first briefly introduce the related works in Section 2. In Section 3, we present the details of our proposed methodology. Datasets and experimental results are described in Section 4, 5. Finally, we discuss our key findings and limitations of our work in Section 6, followed by conclusion in Section 7.

2. Related works

In this section, for brevity, we review only the recent developments in self-supervised and semi-supervised representation learning literature that are closely relevant to our work.

2.1. Self-Supervised learning

Self-supervised learning (SSL) has recently gained momentum in many medical image analysis tasks for reducing the manual annotation burden. These approaches aim to construct different auxiliary pretext tasks, where the supervisory signals are generated within the data. Such self-supervised pretraining of convolutional neural networks (CNN), which are designed to solve these pretext tasks, results in useful visual representations that can be transferred to multiple downstream tasks by fine-tuning with limited labels in a task-specific way. The existing SSL methods in the literature are generally grouped into three categories (Jing and Tian, 2020): context-based, generative-based, and contrastive-based methods.

Among the *context-based* methods, the design of pretext tasks is generally based on domain-specific knowledge or handcrafted according to the data. Examples with application to medical image analysis include image context restoration (Chen et al., 2019), anatomical position prediction (Bai et al., 2019), 3D distance prediction (Spitzer et al., 2018), Rubik’s cube recovery (Zhuang et al., 2019) and image intrinsic spatial offset prediction (Blendowski et al., 2019). Many such pretext tasks are often designed based on ad-hoc heuristics, limiting the generalizability of learned representations. An alternative stream of approach is based on *generative* modeling such as VAE (Kingma and Welling, 2013) or GAN-based models (Dumoulin et al., 2016; Donahue et al., 2016) which implicitly learn representations by minimizing the reconstruction loss in the pixel space. Compared with the discriminative ones, generative approaches are overly focused on pixel-level details, which limits their ability to model complex structures present in an image.

Recently, a new class of discriminative methods is proposed based on *contrastive* learning, which learns to enforce similarities in the latent space between similar/dissimilar pairs (He et al., 2020; Chen et al., 2020; Oord et al., 2018). In such methods, the similarity is defined through maximizing mutual information (Oord

et al., 2018) or with different data augmentations (Chen et al., 2020). Notable technique by Chaitanya et al. (2020) extended the contrastive learning approach (Chen et al., 2020) by utilizing domain and problem-specific cues to segment volumetric medical images on three different MRI datasets. Furthermore, Li et al. (2020b) proposed a patient feature based softmax embedding to learn multi-modal representations for diagnosing retinal diseases. Finally, the contrastive based approach was also extended to histopathology in Lu et al. (2019), by combined attention based multiple instance learning with contrastive predictive coding for weakly supervised histology classification.

2.2. Semi-Supervised learning

The existing semi-supervised learning (SmSL) techniques can be broadly categorized into three groups: i) *adversarial training*-based (Zhang et al., 2017; Diaz-Pinto et al., 2019; Quiros et al., 2019); ii) *graph*-based (Shi et al., 2020; Javed et al., 2020; Aviles-Rivero et al., 2019); and iii) *consistency*-based (Li et al., 2020a; Zhou et al., 2020; Li et al., 2020c; Su et al., 2019; Liu et al., 2020) approaches.

The *adversarial training* based SmSL approaches learn a generative and a discriminate model simultaneously by forcing the discriminator to output class labels instead of estimating the input probability distribution, as in a normal generative adversarial network (GAN). For example, Zhang et al. (2017) proposed a segmentation and evaluation network, where the segmentation network is encouraged to obtain a segmentation mask for unlabeled images; while, the evaluation network is forced to distinguish the segmentation results with the ground truth by assigning different scores. Meanwhile, Quiros et al. (2019) generated pathologically meaningful representations in histopathology to synthesize high-fidelity H&E breast cancer images resembling that of real ones. On the other hand, *graph* based methods construct a graph that establishes a semantic relationship between its neighbors and utilize the transduction of the graph to assign labels to unlabeled data via label propagation. As a typical example, Aviles-Rivero et al. (2019) proposed a graph-based SSL model for chest X-ray classification, where the pseudo labels for unlabeled data are generated using label propagation. In more recent work, Shi et al. (2020) utilized a graph-based self-ensembling approach to minimize the distance between the label prediction and its en-

semble target via consistency cost. In general, such self-ensembling based approaches are shown to be robust to noisy labels compared to other graph-based techniques.

The most recent line of work in SmSL is based on *consistency* regularization, which enforces the consistency of predictions to random perturbations such as data augmentations (French et al., 2017), stochastic regularization (Laine and Aila, 2016; Sajjadi et al., 2016) and adversarial perturbation (Miyato et al., 2018). The most notable method by Tarvainen and Valpola (2017) proposed the mean-teacher framework that averages the model weights instead of the exponential moving average of the label predictions to enhance the quality of consistency targets. These strategies were recently extended to several medical image analysis tasks. For instance, Li et al. (2020c) introduced a transformation consistent self-ensembling model for segmenting medical images. Further, several extensions to mean-teacher have also been explored by enforcing prediction consistency in either region-based (Zhou et al., 2020), relation-based (Liu et al., 2020; Su et al., 2019) or cross-domain based (Li et al., 2020a), which is subjected under various domain-specific perturbations.

3. Methods

An overview of our proposed self-supervised driven consistency training approach is illustrated in Fig. 1. Our framework consists of three main stages: **i)** we pretrain a self-supervised model F_{pre} on an unlabeled set D_{pre} to obtain task-agnostic feature representations; **ii)** we fine-tune the SSL model on a limited amount of labeled data D_{fi} to obtain the task-specific features; and **iii)** we further improve the downstream performance on the target task by using both labeled D_{fi} and unlabeled D_{fu} data in a task-specific semi-supervised manner. For task-specific semi-supervised training, both teacher F_t and student F_s networks are initialized with the fine-tuned model F_{fi} . The main objective is then to optimize the student network, which learns to minimize the supervised loss on the labeled set (D_{fi}) and consistency loss on the unlabeled set (D_{fu}). During consistency training, the teacher network predicts the pseudo label on a weakly augmented unlabeled image, while the student network tries to match this pseudo label by making its prediction on a strongly augmented version of the same unlabeled image. The details are presented next.

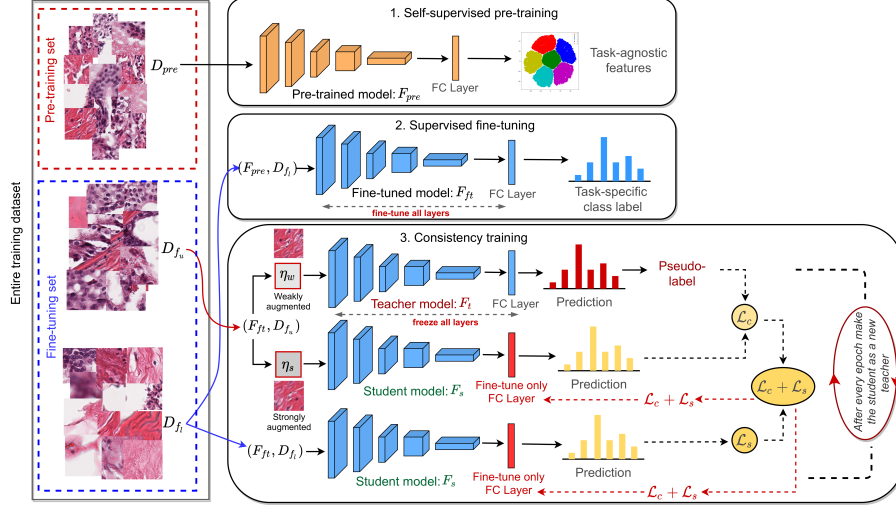


Figure 1: Our self-supervised driven consistency training approach for histopathology image analysis. Our approach consists of three main stages: **i)** First, we pretrain a self-supervised (SSL) model F_{pre} on the unlabeled set D_{pre} to obtain task-agnostic feature representations; **ii)** Second, we fine-tune the pretrained SSL model on a limited amount of labeled data D_{fi} to obtain the task-specific downstream features; and **iii)** Finally, we further improve the downstream performance on the target task by using both labeled (D_{fi}) and unlabeled (D_{fu}) set in a task-specific semi-supervised manner. Both teacher F_t and student F_s networks are initialized with fine-tuned model F_{fi} for consistency training on the target task. The main objective is to optimize the student network, which learns to minimize the supervised loss \mathcal{L}_s on labeled set D_{fi} and consistency loss \mathcal{L}_c on an unlabeled set D_{fu} . The consistency loss is measured between the pseudo labels produced by the teacher network on weakly augmented unlabeled input images with the labels predicted by the student network on a strongly augmented version of the same unlabeled input images. Note: all the above network (F_{pre} , F_{fi} , F_t , F_s) share the same backbone ResNet-18 architecture.

3.1. Self-supervised pretraining of visual representations

The goal of self-supervised pretraining is to learn generic visual representations using unlabeled data that can be transferred to many different downstream tasks by fine-tuning with limited labels in a task-specific way. The self-supervised pretraining is performed by solving a pretext task in a task-agnostic manner, where the labels needed to train the network are generated within the data. Before we begin our proposed SSL approach, we first outline some basics of SSL in detail.

Let us denote the **pretraining set** as $D_{pre} = \{x_i\}_{i=1}^M$ consisting of M **unlabeled** training samples. The aim of SSL is to train a convolutional neural network (convNet) F_{pre} on this unlabeled set D_{pre} to obtain generalized feature representations in a task-agnostic manner. In histopathology, the input $x_i \in \mathbb{R}^{H \times W \times 3}$ denotes the RGB image patch, sampled from a gigapixel WSI, with height (H) and width (W); and $y_i \in C$ is the class label for x_i , with $C = \{0, 1\}$ for classification or \mathbb{R} for regression. Our goal is to learn feature embedding $F_\theta(\cdot)$ in an unsupervised manner that maps an unlabeled set $F_\theta(x_i)$ to a low-

dimensional embedding $F_\theta(x_i) : \mathbb{R}^{H \times W \times 3} \rightarrow \mathbb{R}^d$, with d being the feature dimension, and $F(\cdot)$ denotes the neural network parameterized by θ . Given a set of M training samples $D_{pre} = \{x_i\}_{i=1}^M$, the self-supervised pretraining aims to optimize the following objective:

$$L_{pre} = \min_{\theta} \frac{1}{M} \sum_{i=1}^M \text{loss}(x_i, p_i), \quad (1)$$

where, p_i are the pseudo labels generated automatically from the self-supervised pretext tasks. To this end, we propose a context-based resolution sequence prediction as a domain-specific pretext task to learn generic visual representations, which can be transferred to many different downstream tasks in histopathology.

3.1.1. Resolution sequence prediction (RSP)

Our self-supervised design choice for the “Resolution sequence prediction (**RSP**)” task is inspired by how a pathologist examines a WSI during diagnosis for potential abnormalities. Typically, a pathologist switches multiple times between lower magnification levels for con-

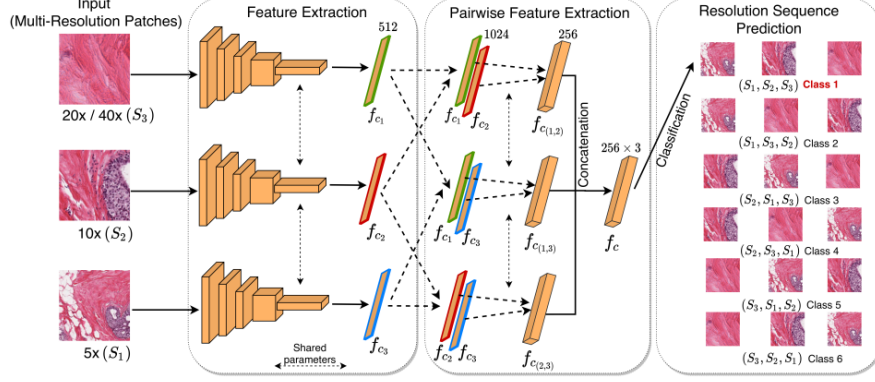


Figure 2: Resolution sequence prediction (RSP) pretext task that we propose for self-supervised representation learning. Given a tuple of three input multi-resolution patches sampled from the $3! = 6$ possible permutations of resolution sequences, we train a ConvNet model $F(\cdot)$ to predict the label $y \in \mathbb{R}^P$ corresponding to the order of resolution sequence, where, $P \in (1, 2, \dots, 6)$. The proposed RSP framework consists of three following stages: **i)** feature extraction; **ii)** pair-wise feature extraction; and **iii)** resolution sequence prediction. Features ($d = 512$) for each input multi-resolution patch are extracted from the convNet model, which are later pair-wise concatenated (to obtain $d = 1024$), followed by learning a 2-layer multi-layer perceptron (MLP) to obtain pair-wise features ($d = 256$). Finally, these pair-wise features are concatenated ($d = 768$), which are then fed to another 2-layer MLP with softmax to predict the resolution sequence order P .

text and higher magnification levels for detail. Such multi-resolution multi-field-of-view (FOV) analysis is possible due to the WSI’s pyramidal nature, where the multiple downsampled versions of the original image are stored in a pyramidal structure. In this work, we exploit this multi-resolution nature of WSIs by proposing a novel self-supervised pretext task - which learns image representations by training convNets to predict the *order* of all possible sequences of resolution that can be created from the input multi-resolution patches. We argue that solving this resolution prediction task will allow CNN to learn useful visual representations that inherently capture both contextual information (at *lower* magnification) and fine-grained details (at *higher* magnification levels).

Specifically, we create 6-tuples of randomly shuffled multi-resolution patches sampled from input WSI. We formulate our resolution sequence prediction task as a *multi-class* classification problem. Formally, we construct a tuple of three concentric multi-resolution RGB image patches $(S_1, S_2, S_3) \in \mathbb{R}^{P \times P \times 3}$ extracted at three different magnification levels, such that the spatial resolution of $S_1 \ll S_2 \ll S_3$ (measured in $\mu\text{m}/\text{px}$). By extracting such multiple concentric same size patches ($P \times P \times 3$), we ensure that the FOV of one image patch (S_3) lies inside the central square region of the other two (S_2, S_1) lower magnification patches. A sample set of multi-resolution

concentric patches are shown in Fig. 2. These sets of patches form an input tuple to our self-supervised RSP framework. For brevity, we only consider a tuple of three input patches from a given WSI, for which $3! = 6$ possible permutations can be constructed (which is referred to as *resolution sequence ordering*), as illustrated in Fig. 2.

To achieve our goal, given an input multi-resolution sequence $x \in (S_1, S_2, S_3)^P \in \mathbb{R}^{P \times P \times 3}$ - among P possible permutations, we aim to train a siamese convNet model (Koch et al., 2015) F_{pre} to predict the label $y \in \mathbb{R}^P$ (i.e., order of resolution sequences over $P \in (1, 2, \dots, 6)$ possible classes), which is given by,

$$F_{pre}(x | \theta) = \{F_{pre}^y(x | \theta)\}_{y=1}^P, \quad (2)$$

where, $F_{pre}^y(x | \theta)$ is the predicted class probability for the input sequence x , with label y , and θ being the learnable parameter of the model $F(\cdot)$. Therefore, given a set of M training samples from the unlabeled set $D_{pre} = \{x_i\}_{i=1}^M$, the convNet model learns to solve the objective function defined in Eq. 1, by minimizing the categorical cross-entropy (CE) loss defined by,

$$\text{loss}(x_i, y_i) = -\log(F_{pre}^y(x_i | \theta)). \quad (3)$$

The proposed RSP framework has **three** main stages: i) feature extraction; ii) pair-wise feature extraction; and iii) resolution sequence prediction. In the *first* stage, we

adopt the siamese based architecture to obtain features for each input multi-resolution patch, where all three network branches share the same parameters. In our work, we adopt the commonly used ResNet-18 model to obtain the features $h_i = F(x_i)$, after the global average pooling layer; where, $h_i \in \mathbb{R}^d$ is a latent vector of dimension 512. An additional crucial part of self-supervised pretraining is preparing the training data. To prevent the model from picking up on low-level cues and learning only trivial features, we make the sequence prediction task more difficult by applying various geometric transformations to the input data. The details of these geometric transformations are discussed thoroughly in Section 4.2. In the *second* stage, we perform pair-wise feature extraction on the extracted feature vector h_i , to capture the intrinsic relationship between the multi-resolution frames. Specifically, we concatenate features of each pair of input patches (i.e., $\text{Concat}(h_1, h_2), \text{Concat}(h_1, h_3), \text{Concat}(h_2, h_3)$) to obtain $h_{ij} \in \mathbb{R}^{d=1024}$ feature vector. Next, we use a 2-layer multi-layer perceptron (MLP) to obtain $z_i = g(h_{ij}) = W_2 \sigma(W_1 h_{ij}) \in \mathbb{R}^{d=256}$; where, σ denotes ReLU and the bias is ignored for simplicity. Finally, in the *third* stage, the pair-wise features (z_i 's) are concatenated, resulting in $d = 256 \times 3$ feature vector. This feature vector is finally fed to another 2-layer MLP with softmax function to predict the order of resolution sequence (i.e., one of 6 possible permutations), as illustrated in Fig. 2.

The most common protocol (Goyal et al., 2019) to evaluate the self-supervised pretrained representations is by training a supervised linear classifier on fixed feature representations, followed by a final evaluation on the test set. In general, most existing SSL approaches utilize the entire task-specific training set D_f to fine-tune the pretrained model on the downstream tasks. However, despite their tremendous success, they still fail to adapt to the new target tasks when the number of labeled training instances is less (Zoph et al., 2020; Yan et al., 2020; Goyal et al., 2019). A recent study by Zoph et al. (2020) reveals that the value of pretraining diminishes with stronger data augmentation and with the use of more task-specific label data. Further, the authors have shown that the self-supervised pretraining benefits only when fine-tuned with limited amounts of labeled data; whereas, the model performance deteriorates using a more extensive label set.

This raises an important **question** to “what degree the SSL works and how much amount of labeled data do we

need to fine-tune the pretrained SSL model”. In this work, we focus on **answering** the above question by performing a set of control experiments by varying the amount of labeled data in both low-data and high-data regimes on three different histopathology datasets. To this end: i) we first supervised fine-tune the pretrained SSL model with varying amounts of labeled data; and ii) we provide an elegant solution based on *teacher-student* consistency paradigm to further improve the downstream performance by exploiting the unlabeled data in a task-specific semi-supervised manner. The details are presented next.

3.2. Supervised fine-tuning

The unsupervised learned representations are now transferred to the downstream task using limited labeled data in a task-specific way. We choose to fine-tune all layers in the pretrained network end-to-end to obtain task-specific representations: $F_{ft}(x_i) = W_{ft} F_{pre}(x_i)$; where, W_{ft} are the weights for the task-specific linear layer. Specifically, we add a linear classifier or a regressor onto the end of the pretrained network (i.e., ResNet-18 (until the global average pooling layer) + 2-layer MLP + Fc) and use limited labeled data to fine-tune the entire network. In order to assess how performance of self-supervised pretrained models varies as we increase the fraction of available labeled data $D_{f_l} = \{(x_i, y_i)\}_{i=1}^{\alpha \times N}$, we choose to look at the effect of keeping just $\alpha \times N$ of the total N available labels in each dataset, where $\alpha \in \{10\%, 25\%, 50\%, 100\%\}$.

3.3. Consistency training

Let us consider the downstream fine-tuning set D_f in each experiment consists of a total of N samples, out of which $\alpha \times N$ are retained as **labeled** inputs $D_{f_l} = \{(x_i, y_i)\}_{i=1}^{\alpha \times N}$, where $\alpha \in \{10\%, 25\%, 50\%, 100\%\}$. In order to maximise the number of unlabeled instances available for training, we use all N samples as **unlabeled** inputs $D_{f_u} = \{x_i\}_{i=1}^N$, i.e., we include all labeled instances D_{f_l} as a part of unlabeled set - discarding their labels, when constructing D_{f_u} .

Our teacher-student consistency training (shown in Fig.1) has **three** following steps:

3.3.1. Initialization

First, we start by initializing both teacher F_t and student F_s network with the supervised fine-tuned model F_{ft}

(as explained in Section 3.2). Both teacher and student are identical networks consisting of ResNet-18 backbone (until the global average pooling layer) + 2-layer MLP + Fc. We freeze the weights of the teacher network across all layers; while the student network consisting of the last 2-layer MLP (Fc1, ReLU, Fc2) and a linear classifier/regressor (Fc) is being trained, keeping the backbone weights (until the output of global average pooling layer) fixed.

3.3.2. Training the student model

Second, we use the teacher network F_t to generate pseudo labels on the deliberately noised unlabeled data D_{fu} . Then, a student network F_s is trained via standard supervised loss (on labeled data) and consistency loss (on unlabeled data). i.e., the supervised loss is evaluated by comparing against the ground truth labels (cross-entropy (CE) for classification / mean squared error (MSE) for regression task); while, the consistency loss (CE for classification / MSE for regression task) is obtained by comparing against the pseudo labels (i.e., logits for regression or one-hot labels for classification) produced by the teacher network. More formally, we aim to minimize the following objective (**total loss**):

$$\min_{\theta} \sum_{i=1}^{\alpha N} \mathcal{L}_s(F_s(x_i; \theta_s), y_i) + \lambda \mathcal{L}_c(\{x_i\}_{i=1}^N; F(\cdot), \theta_t, \eta_w, \theta_s, \eta_s), \quad (4)$$

where, \mathcal{L}_s is the **supervised loss** measured against the labeled inputs and \mathcal{L}_c is the **consistency loss** evaluated between the same unlabeled inputs with different data augmentations. The term λ is the weighting factor which is empirically set as 1, that controls the trade-off between the supervised and consistency loss. $F(\cdot)$ denotes the ConvNet model parameterized by θ , with θ_t and θ_s are the weights of the teacher and student network, respectively; while, η_w and η_s represents the weak and strong data augmentations applied to teacher and student model, respectively.

In each input minibatch, we sample $L = \{(x_i, y_i) : i \in (1, \dots, B)\}$ with B labeled examples drawn from labeled set D_{fl} and $U = \{(x_i) : i \in (1, \dots, \mu B)\}$ with μB unlabeled examples drawn from unlabeled set D_{fu} , such that $\mu B \gg B$. The term μ is a hyperparameter that determines the relative ratio of U and L . Next, we define the **consistency loss**

\mathcal{L}_c for **regression** task as the distance between the prediction of teacher network F_t (with weights θ_t and noise η_w) with the prediction of student network F_s (with weights θ_s and noise η_s):

$$\mathcal{L}_c^{\text{regression}} = \sum_{i=1}^{\mu B} \mathbb{E}_{\eta_w, \eta_s} \|F_t(x_i, \theta_t, \eta_w) - F_s(x_i, \theta_s, \eta_s)\|^2, \quad (5)$$

where, x_i denotes each unlabeled training instance sampled from the unlabeled training set D_{fu} . In contrast, for **classification** task, the consistency loss is calculated via standard cross-entropy (CE) loss defined by:

$$\mathcal{L}_c^{\text{classification}} = \sum_{i=1}^{\mu B} \mathbb{1}\{\max(q_i)\} H(\arg \max(q_i), \hat{q}_i), \quad (6)$$

where, $q_i = p_t(y_i | \eta_w(x_i))$ is the predicted class probability by the teacher network F_t for input x_i applied with **weak augmentation** (η_w) and $\hat{q}_i = p_s(y_i | \eta_s(x_i))$ is the predicted class probability by the student network F_s for input x_i applied with **strong augmentation** (η_s). The term $H(\cdot)$ denotes the CE between two probability distributions and $\arg \max(q_i)$ is the **pseudo label** produced by the teacher network on weakly augmented unlabeled input image $\eta_w(x_i)$. In this work, we leverage two kinds of augmentations: weak and strong. The weak augmentation includes simple horizontal flip and cropping; while for strong augmentation, we use RandAugment technique (Cubuk et al., 2020). The complete list of data augmentations and their parameter settings are listed in Section 4.2.

During each epoch, we only update the weights of the student network while keeping the teacher network weights fixed. The student network weights are updated by learning a 2-layer MLP (Fc1, ReLU, Fc2) with a task-specific linear classifier/regressor on the output of global average pooling layer, with the rest of the layer weights being frozen. The idea of fine-tuning the last layers (i.e., 2-layer MLP and a linear classifier/regressor) of the student model improves the task-specific performance by using both labeled and unlabeled examples in a task-specific manner. This is because the effect of pretraining and most feature re-use happens in the lowest layers of the network, while fine-tuning higher layers change representations that are well adapted to the downstream tasks. This observation was also shown to be consistent in a recent study by Raghu et al. (2019).

3.3.3. Updating the teacher model

At the end of each epoch, the teacher is replaced by the newly trained student $F_t \leftarrow F_s$ and this process is iterated until the model converges. In this way, our teacher-student consistency approach propagates the label information to the unlabeled data by constraining the model predictions to be consistent with the unlabeled data under different data augmentations. The pseudocode for our proposed consistency training is illustrated in Algorithm 1.

4. Experiments

We evaluate the efficacy of our method on one regression and two classification tasks on histopathology benchmark datasets, including BreastPathQ (Martel et al., 2019), Camelyon16 (Bejnordi et al., 2017) and Kather multi-class (Kather et al., 2019). Further, we also show extensive ablation experiments and compare them with state-of-the-art SSL methods by varying different percentages of labeled data.

For baselines, we compare our SSL approach (i.e., RSP) with two other popular SSL methods, including the supervised one: VAE (Kingma and Welling, 2013) (refer, Appendix C), MoCo (He et al., 2020) (refer, Appendix B), and the random weight initialized (supervised). To further evaluate our approach on task-specific consistency training, we fine-tune the same self-supervised pretrained models for the second time using different percentages of task-specific labeled data. In our experiments, we first initialize the teacher-student model with the fine-tuned SSL model trained on different percentages of labeled data (α): 10%, 25%, 50%, and 100% (depicted as “self-supervised pretraining and supervised fine-tuning” in Table 3, 4, 5). Next, we train each of these fine-tuned models again for the second time using labeled and unlabeled samples, again by varying percentages of labeled data (α) and report the final results (depicted as “consistency training (CR)” as shown in Table 3, 4, 5). Note: this experimental setting is kept standard across all three datasets for a fair evaluation.

4.1. Datasets

The distribution of the number of WSI’s and their corresponding patches in all three datasets used for our experiments is shown in Table 1. In this section, we briefly

Algorithm 1: Consistency training pseudocode

Inputs: $L = \{(x_i, y_i) : i \in (1, \dots, B)\}$ with B labeled examples drawn from labeled set D_{f_l}
 $U = \{(x_i) : i \in (1, \dots, \mu B)\}$ with μB unlabeled examples drawn from unlabeled set D_{f_u}
 μ = ratio of unlabeled data
 λ = weighting factor for consistency loss
 F_{f_t} = fine-tuned model
 F_t = teacher model with parameter θ_t
 F_s = student model with parameter θ_s
 η_w = set of weak augmentations
 η_s = set of strong augmentations
 η = set of augmentations applied to labeled data

Initialize: $F_t \leftarrow F_{f_t}$, with weights frozen across entire network
 $F_s \leftarrow F_{f_t}$, with weights frozen until the output of global average pooling layer; and training a 2-layer MLP (Fc1, ReLU, Fc2) + a linear classifier/regressor

```

1 for  $t$  in  $[1, \text{num\_epochs}]$  do
2   for each minibatch  $B$  do
3      $z_{i \in B}^S \leftarrow F_s(\eta(L_{i \in B}))$ 
4      $z_{i \in \mu B}^U \leftarrow F_t(\eta_w(U_{i \in \mu B}))$ 
5      $\hat{z}_{i \in \mu B}^U \leftarrow F_s(\eta_s(U_{i \in \mu B}))$ 
6      $q_{i \in \mu B} = p_t(y_i | \eta_w(U_{i \in \mu B}); \theta_t)$  // prediction computed by  $F_t$ 
7      $\hat{q}_{i \in \mu B} = p_s(y_i | \eta_s(U_{i \in \mu B}); \theta_s)$  // prediction computed by  $F_s$ 
8     supervised loss
9      $\mathcal{L}_s^{\text{classification}} = \frac{1}{|B|} \sum_{i \in B} \log z_i^S [y_i]$ 
10     $\mathcal{L}_s^{\text{regression}} = \frac{1}{|B|} \sum_{i \in B} \|z_i^S - y_i\|^2$ 
11    consistency loss
12     $\mathcal{L}_c^{\text{classification}} = \frac{1}{|\mu B|} \sum_{i \in \mu B} \mathbb{1} \{ \max(q_i) \} H(\arg \max(q_i), \hat{q}_i)$ 
13     $\mathcal{L}_c^{\text{regression}} = \frac{1}{|\mu B|} \sum_{i \in \mu B} \|z_i^U - \hat{z}_i^U\|^2$ 
14    total loss
15    loss  $\leftarrow \mathcal{L}_s + \lambda \mathcal{L}_c$ 
16    update  $\theta_s$  using optimizer
17  end
18   $F_t \leftarrow F_s$  // make student as the new teacher and go back to step 2
19 end
20 return  $\theta_s$ ;
```

describe all three publicly available datasets, whereas the data-specific implementations such as pretraining, fine-tuning, and test splits adopted in our experiments are explained in their respective subsections.

BreastPathQ dataset: This is a publicly available dataset consisting of hematoxylin and eosin (H&E) stained 96 WSI’s of post-NAT-BRCA specimens (Martel et al., 2019; Peikari et al., 2017), which are scanned at 20 \times magnification level (0.5 $lm/pixel$). A set of 2579 patches each with dimension 512 \times 512 are extracted from 69 WSI’s for training, and the remaining 1121 patches are extracted from 25 WSI’s, which are reserved for testing. Two expert pathologists label the images in this dataset according to the percentage of cancer cellularity in each image patch.

Camelyon16 dataset: We performed classification of breast cancer metastases at slide-level on the dataset from Camelyon16 challenge (Bejnordi et al., 2017). This dataset contains 399 H&E stained WSI’s of lymph nodes in the breast, which is split into 270 for training and 129 for testing. The images are acquired from two different scanners with specimen level pixel sizes of 0.226 $\mu m/pixel$ and 0.243 $\mu m/pixel$ spatial resolution and are exhaustively annotated by pathologists.

Kather multiclass dataset: This dataset contains two subsets of patches containing nine tissue classes: adipose, background, debris, lymphocytes, mucus, smooth muscle, normal colon mucosa, cancer-associated stroma, and colorectal cancer epithelium (Kather et al., 2019). Out of the two subsets, the training set consists of 100K image patches of H&E stained colorectal cancer images of 224 \times 224 pixels scanned at 0.5 $\mu m/pixel$ spatial resolution. In contrast, the test set contains 7180 image patches. In this dataset, only patches are made available without access to WSIs.

4.2. Implementation details

We perform all our experiments by selecting ResNet-18 as the backbone feature embedding network on all three datasets. All the experiments were performed on 4 Tesla NVIDIA V100 GPUs, and the entire framework is implemented in PyTorch. We first specify the implementation details common to all datasets, and data-specific implementations are provided in Table 2.

Table 1: The total number of WSI’s and the patches used in each dataset to perform experiments.

Datasets		Pretrain		Fine-tune		Test
		Train	Validation	Train	Validation	
BreastPathQ	WSIs		69		69	25
	Patches	10000	3000	2063	516	1121
Camelyon16	WSIs		60		210	129
	Patches	62156	10000	306303	40000	–
Kather Multi-class	WSIs		–		–	–
	Patches	–	–	80K	20K	7180

For **self-supervised pretraining**. The model is trained for 250 epochs with a batch size of 64. We employ (SGD with Nesterov momentum + Lookahead) optimizer (Zhang et al., 2019), with a momentum of 0.9, weight decay of $1e^{-4}$ and a constant learning rate of 0.01. For Lookahead, we set $k = 5$ and slow weights step size $\alpha = 0.5$. The details of the MoCo and VAE pretraining is provided in Appendix B and Appendix C. The best pretrained model is chosen based on the lowest validation loss for BreastPathQ and Camelyon16 datasets.

We adopt domain-specific data augmentations recommended by Tellez et al. (2019a), including rotations, horizontal flips, scaling, additive Gaussian noise, brightness and contrast perturbations, shifting hue and saturation values in HSV color space, and perturbations in H&E color space. We also add random resized crops, blur, and affine transformations to the previous list. Specifically, we use a rotation factor between $[-90^\circ, +90^\circ]$, scaling factor between $[0.8, 1.2]$, additive Gaussian noise with $[\mu = 0$ and $\sigma = (0, 0.1)]$, affine transformation with translation, scale and rotation limit of $[0.0625, 0.5, 45^\circ]$, respectively, hue and saturation intensity ratio between $[-0.1, 0.1]$ and $[-1, 1]$, respectively, brightness and contrast intensity ratios between $[-0.2, 0.2]$, blurring the input image using a random-sized kernel in the range $[3, 7]$, and randomly resizing and cropping the image patch to its original image size. Finally, we perturb the intensity of hematoxylin and eosin (HED) color channels with a factor of $[-0.035, 0.035]$. We apply all these transformations in sequence by randomly selecting them in each mini-batch to obtain a diverse set of training images.

For **supervised fine-tuning**. We fine-tune the entire pretrained SSL model (all layers) with a linear

Table 2: List of hyperparameters used in our experiments across all three datasets.

	Hyperparameters	BreastPathQ	Camelyon16	Kather Multiclass
Supervised fine-tuning	Epochs	90	90	90
	Batch size	4	16	64
	Learning rate (lr)	0.0001	0.0005	0.00001
	Optimizer	Adam $\beta_1, \beta_2 = (0.9, 0.999)$ $w_d = 1e-4$	SGD with Nesterov momentum of 0.9, $w_d = 1e-4$	Adam $\beta_1, \beta_2 = (0.9, 0.999)$ $w_d = 1e-4$
	Scheduler	MultiStep with lr decay at [30, 60] epochs by 0.1	MultiStep with lr decay at [30, 60] epochs by 0.1	MultiStep with lr decay at [30, 60] epochs by 0.1
	Selection of best model	Lowest validation loss	Highest validation accuracy	Highest validation accuracy
Consistency training	Epochs	90	90	90
	Batch size	4	8	8
	Ratio of unlabeled data (μ)	7	7	7
	Learning rate (lr)	0.0001	0.0005	0.00001
	Optimizer	Adam $\beta_1, \beta_2 = (0.9, 0.999)$ $w_d = 1e-4$	SGD with Nesterov momentum of 0.9, $w_d = 1e-4$	Adam $\beta_1, \beta_2 = (0.9, 0.999)$ $w_d = 1e-4$
	Scheduler	MultiStep with lr decay at [30, 60] epochs by 0.1	MultiStep with lr decay at [30, 60] epochs by 0.1	MultiStep with lr decay at [30, 60] epochs by 0.1
	Selection of best model	Lowest validation loss	Highest validation accuracy	Highest validation accuracy

classifier or a regressor trained on top of the learned representations with limited labeled examples $\alpha = \{10\%, 25\%, 50\%, 100\%\}$ to directly evaluate the performance of RSP, VAE, and MoCo models. In particular, for RSP, we fine-tune the pretrained network (i.e., ResNet-18 (until global average pooling layer) + 2-layer MLP) with a linear layer on the top of $d = (256 \times 3) = 768$ dimensional (d) feature embedding, followed by softmax to obtain task-specific predictions. However, for VAE and MoCo, we fine-tune with a linear layer on the $512 - d$ feature vector. For fine-tuning, we use different sets of hyperparameters for all three datasets, which are provided in Table 2. Further, we include a simple set of augmentations (η as depicted in Algorithm 1), such as rotation, scaling, and random resized crops. For rotation and scaling, we use a factor of $[-90^\circ, +90^\circ]$ and $[0.8, 1.2]$, respectively, and we randomly resize and crop the image patch to its original image size.

For **consistency training**. We use a semi-supervised approach for consistency training by using labeled and unlabeled examples in a task-specific manner. We adopt

the same task-specific fine-tuned model to initialize both teacher and student network, with teacher network weights frozen across all layers; while training a student network with 2-layer MLP (Fc1, ReLU, Fc2) and a task-specific linear layer (classifier/regressor) on the output of global average pooling layer (with rest of the layer weights fixed). All the hyperparameters related to consistency training are shown in Table 2. In our experiments, we initialize the teacher-student model with the fine-tuned SSL model trained on different percentages of labeled data $\alpha = \{10\%, 25\%, 50\%, 100\%\}$. Next, we train each of these fine-tuned models again for the second time using labeled and unlabeled samples, again by varying percentages of labeled data (α), and report the final results.

In our work, we use two kinds of augmentations for consistency training: “**weak**” and “**strong**” augmentation for teacher and student network, respectively. We employ simple transformations such as horizontal flip and random cropping to its original image size as weak augmentations for the teacher network. Whereas for the student network, we adopt a similar set of transformations to the pretraining stage, but with different hyperparameters to strengthen the augmentation severity, which we refer to as strong augmentations. The following are the list of augmentations with different parameters to the pretraining stage: an affine transformation with translation limit of $[0.01, 0.1]$, scale limit of $[0.51, 0.60]$ and rotation of 90° , HSV intensity ratio between $[-1, 1]$ and blurring the input image using a random-sized kernel in the range $[5, 7]$. We apply these augmentations in sequence by randomly selecting them in each mini-batch using the RandAugment technique (Cubuk et al., 2020). In our experiments, we use $N_{Aug} = 7$, $M_g = [1, 10]$ in RandAugment; where, N_{Aug} denotes the number of augmentations to apply sequentially in each mini-batch, and M_g is the magnitude that is sampled within a pre-defined range $[1, 10]$ that controls the severity of distortion in each mini-batch.

4.3. Experiments for BreastPathQ

In this experiment, we train our approach to automatically quantify tumor cellularity (TC) scores in digitized slides of breast cancer images for tumor burden assessment. TC score is defined as the percentage of the total area occupied by the malignant tumor cells in a given image patch (Peikari et al., 2017). For pretraining the SSL approach, we adopted 69 WSI’s of the training set, from

which we randomly extract patches of size (256×256) at $20\times$, $10\times$, and $5\times$ magnification for RSP, while for VAE and MoCo, patches are extracted at $20\times$ magnification. We perform fine-tuning by resizing the image patches to (256×256) on 2579 training image patches (out of which 80% (2063) are reserved for training and 20% (516) for validation), and testing is done on 1121 image patches (as shown in Table 1). To experiment with limited data on the downstream task, we divide the fine-tuning set (i.e., 2063 patches) into four incremental training subsets: $\alpha = \{10\%, 25\%, 50\%, 100\%\}$. Two pathologists annotated each image patch in the test set according to the percentage of cancer cellularity in each image patch. We report the intra-class correlation coefficient (ICC) values between the proposed methods and the two pathologists A and B.

Table 3 presents the ICC values for different methodologies, and the corresponding TC scores produced by each method on sample WSIs of the BreastPathQ test set are shown in Fig. C.3 (shown in Appendix). The consistency training (CR) improved the results of self-supervised pretrained models (VAE, MoCo, and RSP) by a 3% increase in ICC values. Further, all SSL and CR methods (VAE, MoCo, and RSP) seem to exhibit optimal performance, which is close or even outperforming that of supervised baseline (random) on all training subsets. Among all the methods, the RSP+CR achieves the best score of greater than 0.90, which even surpassed the intra-rater agreement score of 0.89 (Akbar et al., 2019). Besides, our obtained TC score of 0.90 on the BreastPathQ test set is superior to state-of-the-art (SOTA) methods (Akbar et al., 2019; Rakhlin et al., 2019), with a maximum score of 0.883. Specifically, our RSP+CR approach achieves a minimum of 4% greater ICC value than VAE+CR and MoCo+CR, and at least 17% improvement in ICC value to the supervised baseline, trained on 10% labeled set (≈ 206 image patches). In contrast, on a complete training set, all CR methods exhibit competitive/similar performance. This indicates that the consistency training improves upon self-supervised pretraining predominantly in the low-data regime.

4.4. Experiments for Camelyon16

This experiment is a slide-based binary classification task to identify the presence of lymph node metastasis in WSIs using only slide-level labels. To experiment with

the limited annotations, we first perform self-supervised pretraining on 60 WSI’s (35 normal and 25 tumor), which are set aside from the original training set. For pretraining, we randomly extract patches of size (256×256) at $40\times$, $20\times$, and $10\times$ magnification for RSP, while for VAE and MoCo, patches are extracted at $40\times$ magnification. Further, the downstream fine-tuning is performed on the randomly extracted patches of size (256×256) from the remaining 210 WSI’s (125 normal and 85 tumor) of the training set, out of which 80% (306.3K patches - 150K tumor + 156.3K normal) are reserved for training and 20% (40K patches - 20K tumor + 20K normal) for validation. We finally evaluate the methods on 129 WSI’s of the test set (as shown in Table 1). We divide the fine-tuning set containing 306.3K patches into four incremental subsets of $\alpha = \{10\%, 25\%, 50\%, 100\%\}$ containing [30.6K, 76.5K, 153.1K, 306.3K] image patches, respectively.

We follow the same post-processing steps as Wang et al. (2016) to obtain slide-level predictions. We first train our proposed models to discriminate patch-level tumor vs. normal patches. We then aggregate these patch-level predictions to create a heat-map of tumor probability over the slide. Next, we extract several features similar to Wang et al. (2016) from the heat map and train a slide-level support vector machine (SVM) classifier to make the slide-level prediction. We compare and evaluate all three SSL pretrained and CR methods with the corresponding supervised baseline. The method’s performance is evaluated in terms of area under the receiver operating characteristic curve (AUC) on a test set containing 129 WSIs. In addition, we also evaluate the binary classification performance (accuracy (Acc)) on the patch-level data containing 40K patches (20K tumor + 20K normal) of the validation set. Further, we perform the statistical significance test by comparing the pairs of AUCs between consistency training and SSL methods using the two-tailed Delong’s test (Sun and Xu, 2014). All differences in AUC value with a p -value < 0.05 were considered significant.

Table 4 presents the AUC scores for predicting slide-level tumor metastasis using different methodologies. On the 10% label regime, RSP and MoCo methods outperformed the supervised baseline, whereas the performance of VAE is significantly decreased compared to other methods. Further, the RSP+CR approach significantly outperforms the RSP by a margin of 2% on 10% and 25% labeled set. The proposed RSP+CR achieves the best

Table 3: Results on BreastPathQ dataset. Predicting the percentage of tumor cellularity (TC) at patch-level (intra-class correlation (ICC) coefficients between two pathologists A and B). The 95% confidence intervals (CI) are shown in square brackets. We bold the best results.

Methods	ICC Coefficient (95% CI)							
	Pathologist A	Pathologist B	Pathologist A	Pathologist B	Pathologist A	Pathologist B	Pathologist A	Pathologist B
% Training Data (α)	10% (206 labels)		25% (516 labels)		50% (1031 labels)		100% (2063 labels)	
Self-supervised pretraining + Supervised fine-tuning								
Random	0.697 [0.67, 0.73]	0.637 [0.60, 0.67]	0.786 [0.76, 0.81]	0.727 [0.70, 0.75]	0.812 [0.79, 0.83]	0.797 [0.77, 0.82]	0.863 [0.85, 0.88]	0.843 [0.83, 0.86]
VAE	0.733 [0.70, 0.76]	0.693 [0.66, 0.72]	0.767 [0.74, 0.79]	0.756 [0.73, 0.78]	0.790 [0.77, 0.81]	0.775 [0.75, 0.80]	0.853 [0.84, 0.87]	0.824 [0.80, 0.84]
MoCo	0.675 [0.64, 0.71]	0.648 [0.61, 0.68]	0.718 [0.69, 0.75]	0.651 [0.62, 0.68]	0.746 [0.72, 0.77]	0.711 [0.68, 0.74]	0.757 [0.73, 0.78]	0.718 [0.69, 0.75]
RSP (ours)	0.701 [0.67, 0.73]	0.667 [0.63, 0.70]	0.796 [0.77, 0.82]	0.734 [0.71, 0.76]	0.842 [0.82, 0.86]	0.834 [0.82, 0.85]	0.884 [0.87, 0.90]	0.872 [0.86, 0.89]
Consistency training (CR)								
Random + CR	0.658 [0.62, 0.69]	0.630 [0.59, 0.66]	0.818 [0.80, 0.84]	0.802 [0.78, 0.82]	0.847 [0.83, 0.86]	0.839 [0.82, 0.86]	0.891 [0.88, 0.90]	0.891 [0.88, 0.90]
VAE + CR	0.771 [0.75, 0.79]	0.727 [0.70, 0.75]	0.842 [0.82, 0.86]	0.826 [0.81, 0.84]	0.866 [0.85, 0.88]	0.857 [0.84, 0.87]	0.884 [0.87, 0.90]	0.864 [0.85, 0.88]
MoCo + CR	0.808 [0.79, 0.83]	0.803 [0.78, 0.82]	0.872 [0.86, 0.89]	0.863 [0.85, 0.88]	0.848 [0.83, 0.86]	0.850 [0.83, 0.87]	0.895 [0.88, 0.91]	0.902 [0.89, 0.91]
RSP + CR (ours)	0.876 [0.86, 0.89]	0.846 [0.83, 0.86]	0.873 [0.86, 0.89]	0.854 [0.84, 0.87]	0.870 [0.86, 0.88]	0.861 [0.84, 0.88]	0.910 [0.90, 0.92]	0.907 [0.90, 0.92]

Table 4: Results on Camelyon16 dataset. Predicting the presence of tumor metastasis at WSI level (AUC) and patch-level classification performance (accuracy). The DeLong method (Sun and Xu, 2014) was used to construct 95% CIs, which are shown in square brackets. The best scores are shown in bold. Note: the patch-level accuracy (Acc) is reported on 40K patches of the validation set.

Methods	AUC		Acc		AUC		Acc		AUC		Acc					
	% Training Data (α)															
	10% (30630 labels)		(4000 labels)		25% (76576 labels)		(10000 labels)		50% (153151 labels)		(20000 labels)		100% (306303 labels)		(40000 labels)	
Self-supervised pretraining + Supervised fine-tuning																
Random	0.804	[0.72 - 0.89]	0.904		0.861	[0.79 - 0.93]	0.936		0.847	[0.77 - 0.92]	0.946		0.865	[0.79 - 0.93]	0.968	
VAE	0.737	[0.64 - 0.83]	0.827		0.814	[0.73 - 0.89]	0.864		0.830	[0.75 - 0.91]	0.906		0.818	[0.73 - 0.90]	0.907	
MoCo	0.895	[0.84 - 0.95]	0.837		0.867	[0.80 - 0.93]	0.895		0.877	[0.81 - 0.94]	0.904		0.857	[0.78 - 0.93]	0.921	
RSP (ours)	0.836	[0.76 - 0.91]	0.898		0.886	[0.83 - 0.94]	0.928		0.861	[0.79 - 0.93]	0.946		0.878	[0.81 - 0.95]	0.953	
Consistency training (CR)																
Random + CR	0.659	[0.54 - 0.77]	0.911		0.782	[0.69 - 0.87]	0.948		0.783	[0.69 - 0.87]	0.955		0.870	[0.80 - 0.94]	0.964	
VAE + CR	0.633	[0.55 - 0.72]	0.828		0.719	[0.63 - 0.81]	0.863		0.741	[0.64 - 0.84]	0.918		0.779	[0.69 - 0.87]	0.928	
MoCo + CR	0.728	[0.63 - 0.82]	0.835		0.742	[0.64 - 0.84]	0.902		0.766	[0.67 - 0.86]	0.929		0.825	[0.75 - 0.90]	0.946	
RSP + CR (ours)	0.855	[0.78 - 0.92]	0.907		0.917	[0.86 - 0.97]	0.935		0.848	[0.77 - 0.93]	0.949		0.882	[0.80 - 0.96]	0.959	

score of 0.917 using a 25% labeled set ($\approx 76K$ patches) compared to the winning method in Camelyon16 challenge (Wang et al., 2016), which obtained an AUC of 0.925 using the fully supervised model trained on millions of image patches. Compared with the unsupervised representation learning methods proposed in Tellez et al. (2019b), our RSP+CR approach trained on 10% labels ($\approx 30K$ patches) outperforms their top-performing BiGAN method by 13% higher AUC trained on 50K labeled samples. We also evaluated our methods performance on the validation set containing 40K patches (20K tumor + 20K normal). Surprisingly, the supervised baseline (Random, Random+CR) outperformed the RSP, RSP+CR methods by a slight margin difference of 0.5% Acc on all percentages of training subsets.

Most importantly, from our experiments on the Camelyon16 dataset, we draw several insights on the generality of our approach on **low-** and **high-labels** training scenar-

ios. On a low-label data regime, *i.e.*, the patch-wise classification task on the validation set, which has training labels ranging from 4K to 40K, we observe that adding consistency training improved the SSL model performance up to a 2% increase in Acc values. In addition, the AUCs of consistency trained models are statistically higher than AUCs of SSL pretrained models, with p -value < 0.02 across 10% and 25% labeled sets. Further, as we increase the number of labeled samples (50% to 100%), adding the consistency training to the Random, VAE, and MoCo pretrained models resulted in a noticeable drop in AUC values. However, the results for the RSP model still improved after consistency training in the high-label data regime, but these differences were not statistically significant. Thus, in general, our approach has been shown to work well in a limited annotation setting, which is highly beneficial in the histopathology domain.

In our experiments, we also observe that the pretrain-

ing performance slightly diminishes with an increase in the amount of labeled data (from 10% (30K) to 100% (306K) labels), which essentially deteriorates the value of pretrained representations, which is consistent with the recent study by Zoph et al. (2020). Overall, our consistency training approach continues to improve the task-specific performance only when trained with less label data, and it is additive to pretraining. Fig. C.4 (shown in Appendix) highlight the tumor probability heat-maps produced by different methodologies. Visually all self-supervised pretrained methods (VAE, MoCo, and RSP) were shown to focus on tumor areas with high probability, while the supervised baseline exhibits slightly lower probability values for the same tumor regions. We observe that most methods successfully identify the macro-metastases (Row 1-3), with a tumor diameter larger than $2mm$, with an excellent agreement with the ground truth annotation. However, the same methods struggle to precisely identify the micro-metastases (Row 4), with tumor diameter smaller than $2mm$, which is generally challenging even for the fully-supervised models.

4.5. Experiments for Kather Multiclass

Due to the unavailability of access to WSIs in this dataset, we could not perform self-supervised pretraining on this dataset. However, we used the SSL pretrained model of Camelyon16 to fine-tune and evaluate the patch-level performance for **feature transferability** between datasets with different tissue types/organs and resolution protocols. In our experiments, the downstream fine-tuning is performed on 100k image patches of the training set and tested on 7180 test set images by resizing the patches to (256×256) pixels.

Table 5 presents the overall Acc and weighted F_1 score (F_1) for classification of 9 colorectal tissue classes using different methodologies. On this dataset, the MoCo+CR approach obtains a new state-of-the-art result with an Acc of 0.990, weighted F_1 score of 0.953 and a macro AUC of 0.997, compared to the previous method (Kather et al., 2019) which obtained an Acc of 0.943. All the consistency trained methods marginally outperform the SSL pretrained models on all the labeled subsets. Further, the CR methods (RSP+CR, MoCo+CR, VAE+CR) outperform the supervised baseline by 3% and 17% increase in Acc and F_1 score, respectively. Finally, our approach has shown 3% improvement in Acc by training on just

10% labels, compared to the previous method (Pati et al., 2020) trained using 100% labels (Acc of 0.951). This underscores that our pretrained approaches are more generalizable to unseen domains with different organs, tissue types, staining, and resolution protocols.

Further, we also observed that the generalizability of RSP is not as good as MoCo for feature transferability between datasets (Camelyon16 \rightarrow Kather Multiclass), as seen in Table 5. We hypothesize that this could be for the following reason: the idea of SSL is to learn generic visual representations that are useful for many downstream tasks across domains. However, in many recent studies (Misra and Maaten, 2020; Purushwalkam and Gupta, 2020; Xiao et al., 2020), it is shown that the generalizability of these pretrained representations is largely dependent on their ability to learn representations that are *invariant* to different image transformations. This invariance to data transformations is inherently learned in MoCo via instance discrimination strategy, which involves treating an image and its transformed versions as one single class. In contrast, the RSP method learns representations that are *covariant* to the pretext task’s transformation (i.e., resolution sequence ordering) rather than invariance to data augmentations (such as in MoCo and SimCLR). In histopathology, these invariances to data augmentations play a vital role in transferring representations to a new target domain, which is consistent with the recent study in (Tellez et al., 2019a). One future work in improving the RSP could be learning representations that are invariant to both data augmentations and pretext image transformations. Some recent methods (Misra and Maaten, 2020; Xiao et al., 2020) have been proposed along these lines to combine domain-specific pretext tasks with contrastive learning to improve the quality of pretrained representations. Nevertheless, a more fundamental understanding of these pretrained representations is still essential to bridge the gap between the handcrafted-based pretext tasks vs. contrastive based SSL methods.

5. Ablation studies

In this section, we perform the ablation experiments to study the importance of two components of our method: (i) ratio of unlabeled data; and (ii) impact of strong augmentations on student network. We choose to perform these ablation studies on $\alpha = 10\%$ labeled data on Breast-PathQ and Camelyon16 datasets due to time constraints.

Table 5: Results on Kather Multiclass dataset. Classification of nine tissue types at patch-level (accuracy (Acc), weighted F_1 score (F_1)). This experiment is performed to assess the generalizability of pretrained features between different tissue types and resolutions. Pretraining is performed on Camelyon16 (Breast) and tested on Kather Multiclass (Colon). We bold the best results.

Methods	Acc	F_1	Acc	F_1	Acc	F_1	Acc	F_1
% Training Data (α)	10% (8000 labels)		25% (20000 labels)		50% (40000 labels)		100% (80000 labels)	
Self-supervised pretraining + Supervised fine-tuning								
Random	0.972	0.873	0.974	0.885	0.979	0.905	0.983	0.920
VAE	0.963	0.835	0.972	0.885	0.980	0.908	0.986	0.934
MoCo	0.982	0.919	0.982	0.919	0.985	0.930	0.975	0.849
RSP (ours)	0.976	0.893	0.975	0.888	0.979	0.907	0.979	0.911
Consistency training (CR)								
Random + CR	0.938	0.670	0.943	0.735	0.941	0.723	0.939	0.707
VAE + CR	0.972	0.876	0.979	0.906	0.978	0.903	0.982	0.915
MoCo + CR	0.987	0.939	0.990	0.953	0.987	0.944	0.983	0.921
RSP + CR (ours)	0.982	0.918	0.982	0.913	0.985	0.930	0.986	0.934

Further, we exclude the Kather Multiclass dataset, as it was used to evaluate the feature transferability between datasets, thus making it less suitable for this extensive study.

5.1. Impact of ratio of unlabeled data

The success of consistency training is mainly attributed to the amount of unlabeled data. From Table 6, we observe marginal to a noticeable improvement in performance, as we increase the ratio of unlabeled (μB) to labeled batch size (B). This is consistent with the recent studies in Xie et al. (2019) and Sohn et al. (2020). For each fold increase in the ratio between unlabeled and labeled samples, the performance improves by at least 2% on BreastPathQ and Camelyon16. However, the performance in BreastPathQ is quite negligible since the number of training samples (2063 patches) is substantially less than Camelyon16 (306K patches). On the other hand, increasing the ratio of unlabeled data while fine-tuning the pretrained model converges faster than training the model from scratch. In essence, a large amount of unlabeled data is always beneficial for better performance during consistency training.

5.2. Impact of strong augmentations on student network

The success of teacher-student consistency training is crucially dependent on the different strong augmentation policies applied to the student network. Table 7 depicts the analysis of the impact of augmentation policies on final performance. In our experiments, we apply each of these augmentations in sequence by randomly selecting them in each mini-batch using the RandAugment (Cubuk

Table 6: Impact of the ratio of unlabeled data (μ). These experiments were performed with $\alpha = 10\%$ labeled data. Note: the intra-class correlation (ICC) coefficient is evaluated between two pathologists A and B for BreastPathQ.

Ratio of Unlabeled Data (μ)	BreastPathQ		Camelyon16	
	ICC (P_A)	ICC (P_B)	AUC	Acc
1	0.871	0.851	0.738	0.904
2	0.871	0.851	0.785	0.903
3	0.876	0.846	0.797	0.907
4	0.876	0.856	0.803	0.911
5	0.880	0.861	0.810	0.914
6	0.882	0.862	0.853	0.907
7	0.876	0.846	0.855	0.907

Table 7: Impact of strong augmentation policies applied to the student network. These number of possible transformations are applied sequentially by randomly selecting them in each mini-batch.

No of Possible Transformations (N_{Aug})	BreastPathQ		Camelyon16	
	ICC (P_A)	ICC (P_B)	AUC	Acc
1	0.883	0.863	0.569	0.895
2	0.883	0.863	0.699	0.898
3	0.882	0.861	0.742	0.899
4	0.878	0.859	0.772	0.903
5	0.881	0.861	0.802	0.901
6	0.880	0.861	0.798	0.903
7	0.876	0.846	0.855	0.907

et al., 2020) technique. We vary the total number of augmentations (N_{Aug}) from value 1 to 7 and examine the effect of strong augmentation policies (applied to the student network) during consistency training. From Table 7, we observe that as we gradually increase the severity of augmentation policies in the student model, there are marginal to noticeable improvements in the performance gain. This improvement is mainly visible when trained on large amounts of unlabeled data (such as Camelyon16),

where there is a minimum 3% improvement in AUC as we increase the augmentation strength. This suggests that adding strong augmentations to the student network is essential to avoid the model being learned just the teacher’s knowledge and gain further improvements in task-specific performance.

6. Discussions

With the advancements in deep learning techniques, current histopathology image analysis methods have shown excellent human-level performance on various tasks such as tumor detection (Campanella et al., 2019), cancer grading (Bulten et al., 2020), and survival prediction (Wulczyn et al., 2020), etc. However, to achieve these satisfactory results, these methods require a large amount of labeled data for training. Acquiring such massive annotations is laborious and tedious in clinical practice. Thus, there is a great potential to explore self/semi-supervised approaches that can alleviate the annotation burden by effectively exploiting the unlabeled data.

Drawing on this spirit, in this work, we propose a self-supervised driven consistency training method for histopathology image analysis by leveraging the unlabeled data in both a task-agnostic and task-specific manner. We first formulate the self-supervised pretraining as the resolution sequence prediction task that learns meaningful visual representations across multiple resolutions in WSI. Next, a teacher-student consistency training is employed to improve the task-specific performance based on prediction consistency with the unlabeled data. Our method is validated on three histology datasets, i.e., BreastPathQ, Camelyon16, and Kather Multiclass, in which our method consistently outperforms other self-supervised methods and also with the supervised baseline under a limited-label regime. Our method has also proven efficacy in transferring pretrained features across different datasets with different tissue types/organs and resolution protocols.

Our work differs from previous consistency based methods in several aspects. Earlier works on consistency training (Sohn et al., 2020; Xie et al., 2019; Tarvainen and Valpola, 2017; Liu et al., 2020; Li et al., 2020c) mainly focused on improving the quality of consistency targets (pseudo labels) by using either of the two strategies: **i)** careful selection of domain-specific data augmen-

tations; or **ii)** selection of better teacher model rather than the simple replication of student network. However, there exist some limitations with the above approaches: First, the predicted pseudo labels for the unlabeled data might be incorrect since the model itself is used to generate them. Suppose, if a higher weight is assigned to these, the quality of learning may be hampered due to misclassification, and the model may suffer from confirmation bias (Arazo et al., 2020). Second, instead of using a converged model (such as pretrained) to generate pseudo labels with high confidence scores, the models are trained from scratch leading to lower accuracy and high entropy. In this work, we overcome these limitations by providing a solution that leverages the advantage of both the above solutions in a simple, efficient manner. The main key difference between our approach and the other existing consistency training methods are two-fold: **i)** we make use of the task-specific fine-tuned model to generate high-confidence (i.e., low-entropy) consistency targets instead of relying on the model being trained; **ii)** we experimentally show that by aggressively injecting noise through various domain-specific data augmentations, the student model is forced to work harder to maintain consistency with the pseudo label produced by teacher model. This ensures that the student network does not merely replicate the teacher’s knowledge.

Despite the excellent performance of our method, there is one main limitation: *i.e.*, if the pseudo labels produced by the teacher network are inaccurate, then the student network is forced to learn from incorrect labels - leading to confirmation bias (Arazo et al., 2020). As a result, the student may not become better than the teacher during consistency training. We solved this issue with RandAugment (Cubuk et al., 2020), a strong data augmentation technique, which we combine with label smoothing (soft pseudo labels) to deal with confirmation bias. This is also consistent with the recent study (Arazo et al., 2020) that showed soft pseudo labels outperform hard pseudo labels when dealing with label noise. However, the bias issue still persists with soft pseudo labels in our application. This is prominently visible in our method, where, compared to self-supervised pretraining (see Fig. C.4, column (c) - (f); Fig. C.3, column (b) - (e)), the consistency trained approaches (see Fig. C.4, column (g) - (j); Fig. C.3, column (f) - (i)) exhibits some low probability (< 0.5) spurious pixels outside the malignant cell boundaries. This

happens because of the naive pseudo labeling produced by the teacher network, which sometimes overfits to incorrect pseudo labels. Further, this issue is reinforced when we attempt to train the student network on unlabeled samples with incorrect pseudo labels leading to confirmation bias. One solution to mitigate this issue is to make the teacher network constantly adapt to the feedback of the student model instead of the teacher model being fixed. This technique has been shown to work well in a recent meta pseudo label method (Pham et al., 2020), where both teacher and student are trained in parallel by making the teacher learn from the reward signal of the student performance on a labeled set. Exploring this idea is beyond the scope of this work, and we will leave this to the practitioner to explore more along these lines.

In general, our proposed self-supervised driven consistency training framework has a great potential to solve the majority of both classification and regression tasks in computational histopathology, where annotation scarcity is a significant issue. Further, our pretrained representations are more generic and easily extended to other downstream multi-tasks, such as segmentation and survival prediction. It is worth further investigating to develop a universal feature encoder in histopathology that can solve many tasks without excessive labeled annotations.

7. Conclusion

In this paper, we present an annotation efficient framework by introducing a novel self-supervised driven consistency training paradigm for histopathology image analysis. The proposed framework utilizes the unlabeled data both in a task-agnostic and task-specific manner to significantly advance the accuracy and robustness of the state-of-the-art self-supervised (SSL) methods. To this end, we first propose a novel task-agnostic self-supervised pretext task by efficiently harnessing the multi-resolution contextual cues present in the histology whole-slide images. We further develop a task-specific teacher-student semi-supervised consistency paradigm to effectively distill the SSL pretrained representations to downstream tasks. This synergistic harness of unlabeled data has been shown to significantly improve the SSL pretrained performance over its supervised baseline under a limited-label regime.

Extensive experiments on three public benchmark datasets across two classification and one regression

based histopathology tasks, *i.e.*, tumor metastasis detection, tissue type classification, and tumor cellularity quantification demonstrate the effectiveness of our proposed approach. Our experiments also showed that our method’s performance is significantly outperforming or even comparable to that of the supervised baseline when trained under limited annotation settings. Furthermore, our approach is more generic and has been shown to generate universal pretrained representations that can be easily adapted to other histopathology tasks and also to other domains without any modifications.

Conflict of interest

ALM is co-founder and CSO of Pathcore. CS, SK and FC have no financial or non-financial conflict of interests.

Acknowledgment

This work was funded by Canadian Cancer Society and Canadian Institutes of Health Research (CIHR). It was also enabled in part by support provided by Compute Canada (www.computeCanada.ca).

Appendix A. Supplementary material

- Fig. C.3 Tumor cellularity scores produced on WSIs of the BreastPathQ test set for 10% labeled data.
- Fig. C.4 Tumor probability heat-maps overlaid on original WSIs from Camelyon16 test set predicted from 10% labeled data.

Appendix B. Momentum contrast (MoCo)

Momentum Contrast model (MoCo) (He et al., 2020) is one of the most popular self-supervised models that even outperforms supervised baseline models. Given a data point x in a dataset, MoCo samples a positive pair k_+ and N negative pairs k_-^1, \dots, k_-^N . MoCo is trained with infoNCE loss (Oord et al., 2018), defined as

$$L_{infoNCE} = -\mathbb{E}_{x \sim p(x)} \left[\frac{\exp(F_q(x) \cdot F_k(k_+)/\tau)}{\sum_{i=1}^N \exp(F_q(x) \cdot F_k(k_-^i)/\tau)} \right], \quad (\text{B.1})$$

where, F_q and F_k are neural networks, and τ is a hyperparameter for temperature. This is a log loss of a softmax

classifier which minimizes the difference between the representations $F_q(x)$ and its positive pair $F_k(k_+)$ while maximizing the differences between $F_q(x)$ and negative pairs $F_k(k_-^{1,\dots,N})$. Note that minimizing L_{infoNCE} maximizes the lower bound for mutual information between x and k_+ (Oord et al., 2018). However, the bound is not tight for a small number of N ; therefore, in practice, we need to use a large number of negative samples for each iteration. However, as this is not practical for computational efficiency, MoCo maintains a large queue of encoded data. At each training iteration, the entire mini-batch consisting of a positive sample and negative samples are inserted into the queue. Therefore, we use the entire queue (except the positive sample) as the set of negatives for the infoNCE loss. One of the key observation made by MoCo is that this can be problematic if the encoder F changes too quickly, as this would cause the discrepancy between the distribution of the samples in the queue and the new samples to be quite different, and the classifier can easily decrease the loss. To solve this problem, MoCo uses two networks: the encoder F_q with parameters θ_q and the momentum encoder F_k with parameters θ_k . F_k is not trained with the infoNCE loss but is updated with momentum parameter m :

$$\theta_k = m \theta_k + (1 - m) \theta_q, \quad (\text{B.2})$$

after each training iteration. We use the queue size of 8192 and m of 0.999, and adopt multiple augmentation schemes. In each training iteration, for each data x , we *randomly* i) jitter the brightness, contrast, saturation, and hue by $0.6 \sim 1.4$, ii) rotate it by $0 \sim 360$ degrees, iii) flip vertically & horizontally, and iv) crop with an area in the range $0.7 \sim 1$ and stretch to the original size.

Appendix C. Variational autoencoder (VAE)

Variational autoencoder (VAE) (Kingma and Welling, 2013) is an unsupervised machine learning model that is often used for dimensionality reduction and image generation. The model contains an encoder and a decoder, with a latent space that has a dimension smaller than the input data. The reduction in dimension on the latent space helps extract the prominent information in the original data. Unlike the vanilla autoencoders, VAE assumes that input data comes from some latent distribution $z \sim N(0, I)$. The encoder estimates the mean (μ) and variance (σ^2) of the data in the latent space, and the decoder samples a point from

the distribution for data reconstruction. The assumption of z following a normal distribution and the stochastic property of the latent vector force the model to create a continuous latent space with similar data closer in the space. This resolves the model overfitting due to irregularities in the latent space often observed in the conventional autoencoder. The learning rule of VAE is to maximize the evidence lower bound (ELBO),

$$ELBO = E_{z \sim q(z|x)} \log p(x|z) - KL(q(z|x) \parallel p(z)) \leq \log p(x), \quad (\text{C.1})$$

where, q is the approximate posterior distribution of $p(z|x)$. The *first* term describes the reconstruction loss of the autoencoder model. The *second* term is can be seen as a regularizer that forces the approximate latent distribution to be close to $N(0, I)$. Standard stochastic gradient descent methods cannot directly apply to the model because of the stochastic property of the latent vector. The solution, called the reparameterization trick, is to introduce a new random variable $\epsilon \sim N(0, I)$ as the model input and set the latent vector to $z = \mu(x) + \sigma^{1/2}(x) \cdot \epsilon$. This allows all model parameters to be deterministic.

For our VAE model, we use a ResNet-18 model to encode input image of size 256×256 to a latent vector of size 512. Then, we use the generator from the BigGAN model (Brock et al., 2018) to reconstruct the latent vector back to the original image.

References

- Akbar, S., Peikari, M., Salama, S., Panah, A.Y., Nofech-Mozes, S., Martel, A.L., 2019. Automated and manual quantification of tumour cellularity in digital slides for tumour burden assessment. *Scientific Reports* 9, 1–9.
- Arazo, E., Ortego, D., Albert, P., O’Connor, N.E., McGuinness, K., 2020. Pseudo-labeling and confirmation bias in deep semi-supervised learning, in: 2020 International Joint Conference on Neural Networks (IJCNN), pp. 1–8.
- Aviles-Rivero, A.I., Papadakis, N., Li, R., Sellars, P., Fan, Q., Tan, R.T., Schönlieb, C.B., 2019. Graphx-net: Chest x-ray classification under extreme minimal supervision. *arXiv preprint arXiv:1907.10085*.
- Bai, W., Chen, C., Tarroni, G., Duan, J., Guitton, F., Petersen, S.E., Guo, Y., Matthews, P.M., Rueckert, D.,

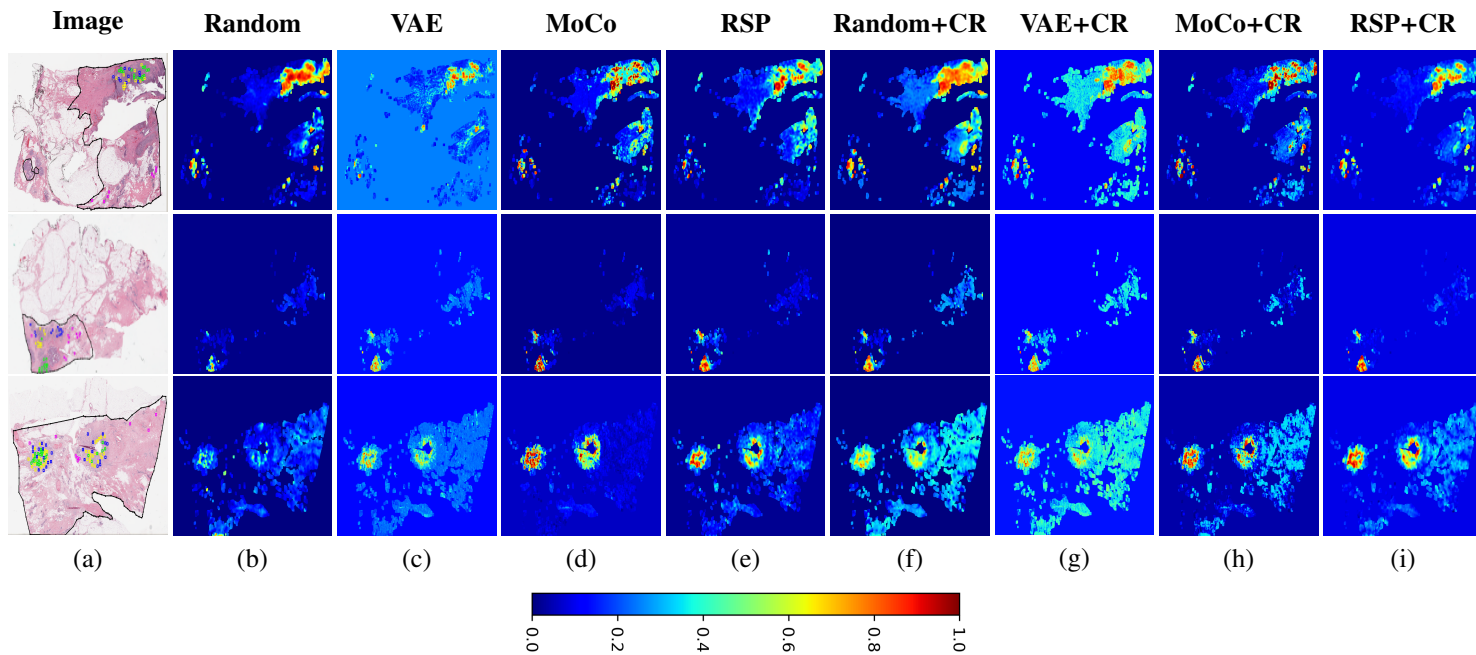


Figure C.3: TC scores produced on WSIs of the BreastPathQ test set for 10% labeled data. (a) Original WSI overlaid with ground truth mask (annotation labels with pink square boxes denote 0% cellularity and green square boxes indicate 100% cellularity); (b) – (e) corresponds to TC score produced by random (supervised), VAE, MoCo, and RSP approach, respectively; (f) – (i) corresponds to TC score produced by random+CR (supervised), VAE+CR, MoCo+CR, and RSP+CR methods, respectively. The color blue denotes healthy (0% TC), and red denotes malignant (100% TC).

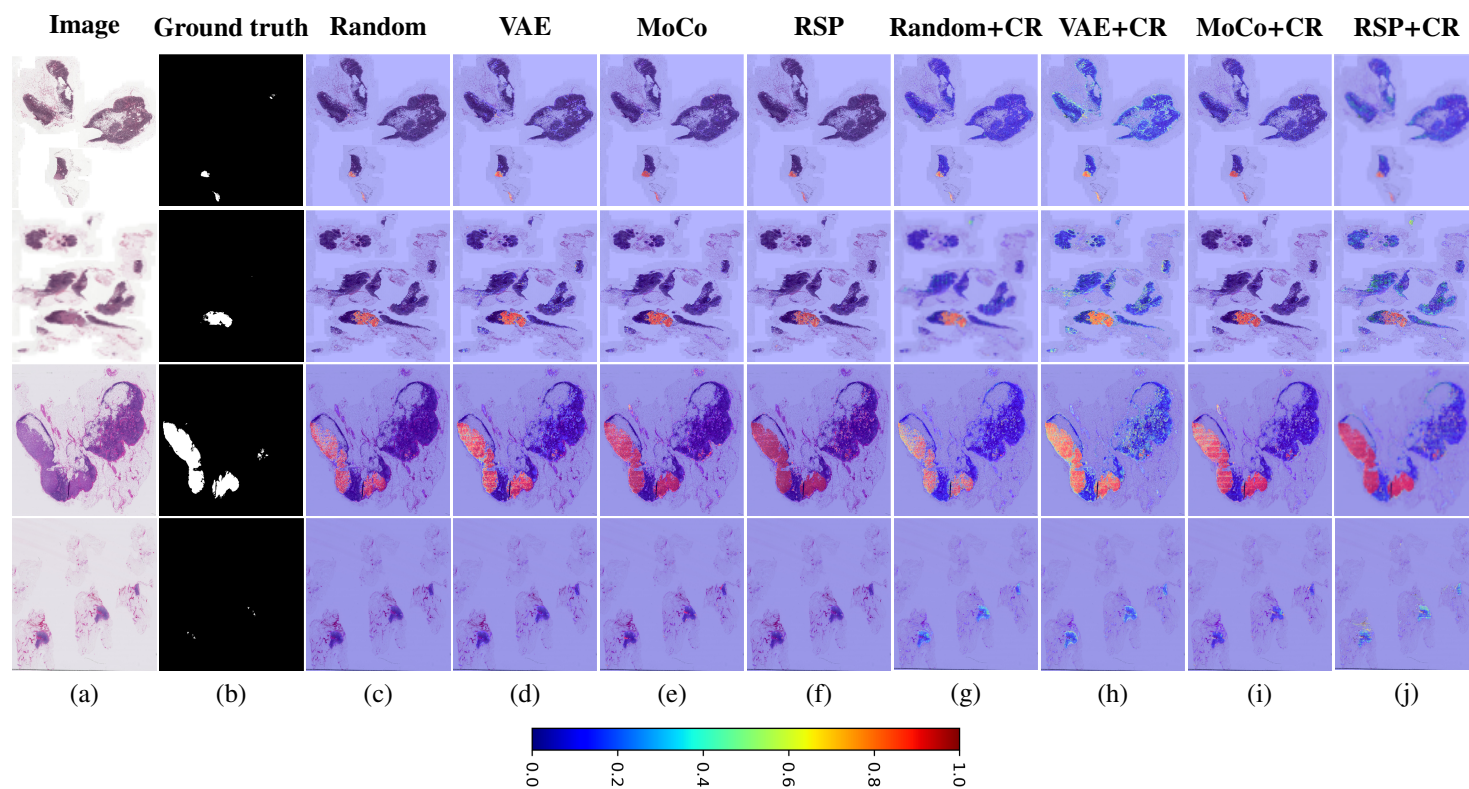


Figure C.4: Tumor probability heat-maps overlaid on original WSIs from Camelyon16 test set predicted from 10% labeled data. (a) Original WSI; (b) Ground truth annotation mask; (c) – (f) corresponds to tumor probability produced by random (supervised), VAE, MoCo, and RSP approach, respectively; (g) – (i) corresponds to tumor probability produced by random+CR (supervised), VAE+CR, MoCo+CR, and RSP+CR methods, respectively. The first three rows correspond to examples of macro-metastases (tumor cell cluster diameter $\geq 2mm$), while the last row corresponds to micro-metastases (tumor cell cluster diameter from $> 0.2mm$ to $< 2mm$). The color blue denotes healthy regions, and red denotes tumor regions.

2019. Self-supervised learning for cardiac mr image segmentation by anatomical position prediction, in: International Conference on Medical Image Computing and Computer-Assisted Intervention, pp. 541–549.
- Bejnordi, B.E., Veta, M., Van Diest, P.J., Van Ginneken, B., Karssemeijer, N., Litjens, G., Van Der Laak, J.A., Hermesen, M., Manson, Q.F., Balkenhol, M., et al., 2017. Diagnostic assessment of deep learning algorithms for detection of lymph node metastases in women with breast cancer. *JAMA* 318, 2199–2210.
- Bera, K., Schalper, K.A., Rimm, D.L., Velcheti, V., Madabhushi, A., 2019. Artificial intelligence in digital pathology—new tools for diagnosis and precision oncology. *Nature Reviews Clinical Oncology* 16, 703–715.
- Blendowski, M., Nickisch, H., Heinrich, M.P., 2019. How to learn from unlabeled volume data: self-supervised 3d context feature learning, in: International Conference on Medical Image Computing and Computer-Assisted Intervention, pp. 649–657.
- Brock, A., Donahue, J., Simonyan, K., 2018. Large scale gan training for high fidelity natural image synthesis. *arXiv preprint arXiv:1809.11096*.
- Bulten, W., Pinckaers, H., van Boven, H., Vink, R., de Bel, T., van Ginneken, B., van der Laak, J., Hulsbergen-van de Kaa, C., Litjens, G., 2020. Automated deep-learning system for gleason grading of prostate cancer using biopsies: a diagnostic study. *The Lancet Oncology* 21, 233–241.
- Campanella, G., Hanna, M.G., Geneslaw, L., Miraflor, A., Silva, V.W.K., Busam, K.J., Brogi, E., Reuter, V.E., Klimstra, D.S., Fuchs, T.J., 2019. Clinical-grade computational pathology using weakly supervised deep learning on whole slide images. *Nature Medicine* 25, 1301–1309.
- Chaitanya, K., Erdil, E., Karani, N., Konukoglu, E., 2020. Contrastive learning of global and local features for medical image segmentation with limited annotations. *arXiv preprint arXiv:2006.10511*.
- Chapelle, O., Schölkopf, B., Zien, A., 2010. *Semi-Supervised Learning*. 1st ed., The MIT Press.
- Chen, L., Bentley, P., Mori, K., Misawa, K., Fujiwara, M., Rueckert, D., 2019. Self-supervised learning for medical image analysis using image context restoration. *Medical Image Analysis* 58, 101539.
- Chen, T., Kornblith, S., Norouzi, M., Hinton, G., 2020. A simple framework for contrastive learning of visual representations. *arXiv preprint arXiv:2002.05709*.
- Cubuk, E.D., Zoph, B., Shlens, J., Le, Q.V., 2020. RandAugment: Practical automated data augmentation with a reduced search space, in: Proceedings of the IEEE/CVF Conference on Computer Vision and Pattern Recognition Workshops, pp. 702–703.
- Diaz-Pinto, A., Colomer, A., Naranjo, V., Morales, S., Xu, Y., Frangi, A.F., 2019. Retinal image synthesis and semi-supervised learning for glaucoma assessment. *IEEE Transactions on Medical Imaging* 38, 2211–2218.
- Donahue, J., Krähenbühl, P., Darrell, T., 2016. Adversarial feature learning. *arXiv preprint arXiv:1605.09782*.
- Dumoulin, V., Belghazi, I., Poole, B., Mastropietro, O., Lamb, A., Arjovsky, M., Courville, A., 2016. Adversarially learned inference. *arXiv preprint arXiv:1606.00704*.
- French, G., Mackiewicz, M., Fisher, M., 2017. Self-ensembling for visual domain adaptation. *arXiv preprint arXiv:1706.05208*.
- Goyal, P., Mahajan, D., Gupta, A., Misra, I., 2019. Scaling and benchmarking self-supervised visual representation learning, in: Proceedings of the IEEE International Conference on Computer Vision, pp. 6391–6400.
- He, K., Fan, H., Wu, Y., Xie, S., Girshick, R., 2020. Momentum contrast for unsupervised visual representation learning, in: Proceedings of the IEEE Conference on Computer Vision and Pattern Recognition, pp. 9729–9738.
- Hinton, G., Vinyals, O., Dean, J., 2015. Distilling the knowledge in a neural network. *arXiv preprint arXiv:1503.02531*.

- Huang, G., Sun, Y., Liu, Z., Sedra, D., Weinberger, K.Q., 2016. Deep networks with stochastic depth, in: European Conference on Computer Vision, pp. 646–661.
- Javed, S., Mahmood, A., Fraz, M.M., Koohbanani, N.A., Benes, K., Tsang, Y.W., Hewitt, K., Epstein, D., Snead, D., Rajpoot, N., 2020. Cellular community detection for tissue phenotyping in colorectal cancer histology images. *Medical Image Analysis* , 101696.
- Jing, L., Tian, Y., 2020. Self-supervised visual feature learning with deep neural networks: A survey. *IEEE Transactions on Pattern Analysis and Machine Intelligence* , 1–1.
- Kather, J.N., Krisam, J., Charoentong, P., Luedde, T., Herpel, E., Weis, C.A., Gaiser, T., Marx, A., Valous, N.A., Ferber, D., et al., 2019. Predicting survival from colorectal cancer histology slides using deep learning: A retrospective multicenter study. *PLoS medicine* 16, e1002730.
- Kim, J., Hur, Y., Park, S., Yang, E., Hwang, S.J., Shin, J., 2020. Distribution aligning refinery of pseudo-label for imbalanced semi-supervised learning. *arXiv preprint arXiv:2007.08844* .
- Kingma, D.P., Welling, M., 2013. Auto-encoding variational bayes. *arXiv preprint arXiv:1312.6114* .
- Koch, G., Zemel, R., Salakhutdinov, R., 2015. Siamese neural networks for one-shot image recognition, in: *ICML Deep Learning Workshop*.
- Laine, S., Aila, T., 2016. Temporal ensembling for semi-supervised learning. *arXiv preprint arXiv:1610.02242* .
- Lee, D.H., 2013. Pseudo-label: The simple and efficient semi-supervised learning method for deep neural networks, in: *Workshop on challenges in representation learning, ICML*, pp. 1–6.
- Li, K., Wang, S., Yu, L., Heng, P.A., 2020a. Dual-teacher: Integrating intra-domain and inter-domain teachers for annotation-efficient cardiac segmentation. *arXiv preprint arXiv:2007.06279* .
- Li, X., Jia, M., Islam, M.T., Yu, L., Xing, L., 2020b. Self-supervised feature learning via exploiting multi-modal data for retinal disease diagnosis. *IEEE Transactions on Medical Imaging* .
- Li, X., Yu, L., Chen, H., Fu, C.W., Xing, L., Heng, P.A., 2020c. Transformation-consistent self-ensembling model for semisupervised medical image segmentation. *IEEE Transactions on Neural Networks and Learning Systems* .
- Litjens, G., Kooi, T., Bejnordi, B.E., Setio, A.A.A., Ciompi, F., Ghafoorian, M., Van Der Laak, J.A., Van Ginneken, B., Sánchez, C.I., 2017. A survey on deep learning in medical image analysis. *Medical Image Analysis* 42, 60–88.
- Liu, Q., Yu, L., Luo, L., Dou, Q., Heng, P.A., 2020. Semi-supervised medical image classification with relation-driven self-ensembling model. *IEEE Transactions on Medical Imaging* .
- Lu, M.Y., Chen, R.J., Wang, J., Dillon, D., Mahmood, F., 2019. Semi-supervised histology classification using deep multiple instance learning and contrastive predictive coding. *arXiv preprint arXiv:1910.10825* .
- Madabhushi, A., Lee, G., 2016. Image analysis and machine learning in digital pathology: Challenges and opportunities. *Medical Image Analysis* 33, 170–175.
- Martel, A.L., Nofech-Mozes, S., Salama, S., Akbar, S., Peikari, M., 2019. Assessment of residual breast cancer cellularity after neoadjuvant chemotherapy using digital pathology [data set]. <https://doi.org/10.7937/TCIA.2019.4YIBTJNO> .
- Misra, I., Maaten, L.v.d., 2020. Self-supervised learning of pretext-invariant representations, in: *Proceedings of the IEEE Conference on Computer Vision and Pattern Recognition*, pp. 6707–6717.
- Miyato, T., Maeda, S.i., Koyama, M., Ishii, S., 2018. Virtual adversarial training: a regularization method for supervised and semi-supervised learning. *IEEE Transactions on Pattern Analysis and Machine Intelligence* 41, 1979–1993.

- Oord, A.v.d., Li, Y., Vinyals, O., 2018. Representation learning with contrastive predictive coding. arXiv preprint arXiv:1807.03748 .
- Pati, P., Foncubierta-Rodríguez, A., Goksel, O., Gabrani, M., 2020. Reducing annotation effort in digital pathology: A co-representation learning framework for classification tasks. *Medical Image Analysis* 67, 101859.
- Peikari, M., Salama, S., Nofech-Mozes, S., Martel, A.L., 2017. Automatic cellularity assessment from post-treated breast surgical specimens. *Cytometry Part A* 91, 1078–1087.
- Pham, H., Xie, Q., Dai, Z., Le, Q.V., 2020. Meta pseudo labels. arXiv preprint arXiv:2003.10580 .
- Purushwalkam, S., Gupta, A., 2020. Demystifying contrastive self-supervised learning: Invariances, augmentations and dataset biases. arXiv preprint arXiv:2007.13916 .
- Quiros, A.C., Murray-Smith, R., Yuan, K., 2019. Pathology gan: learning deep representations of cancer tissue. arXiv preprint arXiv:1907.02644 .
- Raghu, M., Zhang, C., Kleinberg, J., Bengio, S., 2019. Transfusion: Understanding transfer learning for medical imaging, in: *Advances in Neural Information Processing Systems*, pp. 3347–3357.
- Rakhlin, A., Tiulpin, A., Shvets, A.A., Kalinin, A.A., Iglovikov, V.I., Nikolenko, S., 2019. Breast tumor cellularity assessment using deep neural networks, in: *Proceedings of the IEEE International Conference on Computer Vision Workshops*, pp. 0–0.
- Rebuffi, S.A., Ehrhardt, S., Han, K., Vedaldi, A., Zisserman, A., 2020. Semi-supervised learning with scarce annotations, in: *Proceedings of the IEEE Conference on Computer Vision and Pattern Recognition Workshops*, pp. 762–763.
- Sajjadi, M., Javanmardi, M., Tasdizen, T., 2016. Regularization with stochastic transformations and perturbations for deep semi-supervised learning, in: *Advances in Neural Information Processing Systems*, pp. 1163–1171.
- Shi, X., Su, H., Xing, F., Liang, Y., Qu, G., Yang, L., 2020. Graph temporal ensembling based semi-supervised convolutional neural network with noisy labels for histopathology image analysis. *Medical Image Analysis* 60, 101624.
- Sohn, K., Berthelot, D., Li, C.L., Zhang, Z., Carlini, N., Cubuk, E.D., Kurakin, A., Zhang, H., Raffel, C., 2020. Fixmatch: Simplifying semi-supervised learning with consistency and confidence. arXiv preprint arXiv:2001.07685 .
- Spitzer, H., Kiwitz, K., Amunts, K., Harmeling, S., Dickscheid, T., 2018. Improving cytoarchitectonic segmentation of human brain areas with self-supervised siamese networks, in: *International Conference on Medical Image Computing and Computer-Assisted Intervention*, pp. 663–671.
- Srinidhi, C.L., Ciga, O., Martel, A.L., 2021. Deep neural network models for computational histopathology: A survey. *Medical Image Analysis* 67, 101813.
- Srivastava, N., Hinton, G., Krizhevsky, A., Sutskever, I., Salakhutdinov, R., 2014. Dropout: a simple way to prevent neural networks from overfitting. *The Journal of Machine Learning Research* 15, 1929–1958.
- Su, H., Shi, X., Cai, J., Yang, L., 2019. Local and global consistency regularized mean teacher for semi-supervised nuclei classification, in: *International Conference on Medical Image Computing and Computer-Assisted Intervention*, pp. 559–567.
- Sun, X., Xu, W., 2014. Fast implementation of delong’s algorithm for comparing the areas under correlated receiver operating characteristic curves. *IEEE Signal Processing Letters* 21, 1389–1393.
- Tarvainen, A., Valpola, H., 2017. Mean teachers are better role models: Weight-averaged consistency targets improve semi-supervised deep learning results, in: *Advances in Neural Information Processing Systems*, pp. 1195–1204.
- Tellez, D., Litjens, G., Bándi, P., Bulten, W., Bokhorst, J.M., Ciompi, F., van der Laak, J., 2019a. Quantifying

- the effects of data augmentation and stain color normalization in convolutional neural networks for computational pathology. *Medical Image Analysis* 58, 101544.
- Tellez, D., Litjens, G., van der Laak, J., Ciompi, F., 2019b. Neural image compression for gigapixel histopathology image analysis. *IEEE Transactions on Pattern Analysis and Machine Intelligence*.
- Wang, D., Khosla, A., Gargeya, R., Irshad, H., Beck, A.H., 2016. Deep learning for identifying metastatic breast cancer. *arXiv preprint arXiv:1606.05718*.
- Wulczyn, E., Steiner, D.F., Xu, Z., Sadhwani, A., Wang, H., Flament-Auvigne, I., Mermel, C.H., Chen, P.H.C., Liu, Y., Stumpe, M.C., 2020. Deep learning-based survival prediction for multiple cancer types using histopathology images. *PLoS One* 15, e0233678.
- Xiao, T., Wang, X., Efros, A.A., Darrell, T., 2020. What should not be contrastive in contrastive learning. *arXiv preprint arXiv:2008.05659*.
- Xie, Q., Dai, Z., Hovy, E., Luong, M.T., Le, Q.V., 2019. Unsupervised data augmentation for consistency training. *arXiv preprint arXiv:1904.12848*.
- Yan, X., Misra, I., Gupta, A., Ghadiyaram, D., Mahajan, D., 2020. Clusterfit: Improving generalization of visual representations, in: *Proceedings of the IEEE Conference on Computer Vision and Pattern Recognition*, pp. 6509–6518.
- Zhai, X., Oliver, A., Kolesnikov, A., Beyer, L., 2019. S4L: Self-supervised semi-supervised learning, in: *Proceedings of the IEEE International Conference on Computer Vision*, pp. 1476–1485.
- Zhang, M., Lucas, J., Ba, J., Hinton, G.E., 2019. Lookahead optimizer: k steps forward, 1 step back, in: *Advances in Neural Information Processing Systems*, pp. 9597–9608.
- Zhang, Y., Yang, L., Chen, J., Fredericksen, M., Hughes, D.P., Chen, D.Z., 2017. Deep adversarial networks for biomedical image segmentation utilizing unannotated images, in: *International Conference on Medical Image Computing and Computer-Assisted Intervention*, pp. 408–416.
- Zhou, Y., Chen, H., Lin, H., Heng, P.A., 2020. Deep semi-supervised knowledge distillation for overlapping cervical cell instance segmentation. *arXiv preprint arXiv:2007.10787*.
- Zhuang, X., Li, Y., Hu, Y., Ma, K., Yang, Y., Zheng, Y., 2019. Self-supervised feature learning for 3d medical images by playing a rubik’s cube, in: *International Conference on Medical Image Computing and Computer-Assisted Intervention*, pp. 420–428.
- Zoph, B., Ghiasi, G., Lin, T.Y., Cui, Y., Liu, H., Cubuk, E.D., Le, Q.V., 2020. Rethinking pre-training and self-training. *arXiv preprint arXiv:2006.06882*.